

## The Ocean's Skin Layer in the Tropics

Oliver Wurl<sup>1</sup> , William M. Landing<sup>2</sup> , Nur Ili Hamizah Mustaffa<sup>1</sup> , Mariana Ribas-Ribas<sup>1</sup> , Carson Riggs Witte<sup>3</sup> , and Christopher J. Zappa<sup>3</sup> 

## Key Points:

- Tropical ocean is ubiquitously covered with a saline skin layer
- Freshening by precipitation is compensated by wind-driven vertical mixing
- Denser skin layer can float on top of less dense bulk water

## Supporting Information:

- Supporting Information S1
- Figure S1
- Figure S2
- Figure S3
- Figure S4
- Figure S5
- Figure S6
- Figure S7
- Figure S8

## Correspondence to:

O. Wurl,  
oliver.wurl@uni-oldenburg.de

## Citation:

Wurl, O., Landing, W. M., Mustaffa, N. I. H., Ribas-Ribas, M., Witte, C. R., & Zappa, C. J. (2019). The ocean's skin layer in the tropics. *Journal of Geophysical Research: Oceans*, 124. <https://doi.org/10.1029/2018JC014021>

Received 27 MAR 2018

Accepted 6 DEC 2018

Accepted article online 11 DEC 2018

<sup>1</sup>Institute for Chemistry and Biology of the Marine Environment, Carl von Ossietzky University of Oldenburg, Wilhelmshaven, Germany, <sup>2</sup>Department of Earth, Ocean, and Atmospheric Science, Florida State University, Tallahassee, FL, USA, <sup>3</sup>Lamont-Doherty Earth Observatory, Columbia University, Palisades, NY, USA

**Abstract** We provide a large data set on salinity anomalies in the ocean's skin layer together with temperature anomalies and meteorological forcing. We observed an average salinity anomaly of  $0.40 \pm 0.41$  practical salinity unity ( $n = 23,743$ ), and in 83% of the observations the salinity anomaly was positive; that is, the skin layer was more saline. Temperature anomalies determined by an infrared camera were  $-0.23 \pm 0.28$  °C (upper 20- $\mu$ m layer in reference to nominal 1-mm depth) and slightly warmer with  $-0.19 \pm 0.25$  °C in an upper 80- $\mu$ m layer in reference to 1-m depth. In 75% of the observations, our data confirmed the presence of a cooler skin layer. Light rain rates ( $<4$  mm/hr) induced an immediate freshening by 0.25 practical salinity unit in the skin layer without any effect in the mixed layer at 1-m depth. Vertical mixing by strong winds (12 m/s) masked freshening during a heavy rain fall (47 mm/hr) by the intrusion of saltier deeper waters, but a freshening was observed after the wind and rain calmed down. We computed density anomalies, which suggest that denser skin layers can remain afloat up to a density anomaly of 1.3 g/L, likely due to the interfacial tension between the skin layer and underlying bulk water. It implies that salinization by evaporation regulates buoyancy fluxes, a key process for the exchange of climate-relevant gases and heat between the ocean and atmosphere.

**Plain Language Summary** We provide a very large data set of high-resolution in situ observations of the saline skin layer. The major finding is that the ocean's skin layer is more saline than the underlying bulk water in the tropical Pacific, despite the fact that in this region the freshwater flux in and out of the ocean is dominated by precipitation rather than evaporation. We observed that salinity anomalies in the skin layer are very dynamic and that freshwater input by precipitation can be accompanied by wind-driven mixing. During a rain event, we observed that salting by evaporation and vertical mixing is twofold faster than freshening by dilution with rainwater. This knowledge is essential to interpret salinity data from satellites with respect to tracing freshwater fluxes over the ocean.

## 1. Introduction

Despite the vast capacity of the ocean to adsorb and release heat and climate-relevant gases, it is well known that the ocean is changing in terms of warming, rising sea levels, and ocean acidification (Santos et al., 2016). However, the near-surface layer (upper 5 m) has been widely neglected in ocean and climate science, despite its obvious role in controlling the extent and distribution of those changes as a critical element of the ocean-atmosphere system. It includes the skin layer, also referred to as the sea surface microlayer (see definition by Hunter, 2005), representing the interfacial boundary layer (up to 1,000  $\mu$ m in thickness) between the ocean and the atmosphere on a global scale (Wurl et al., 2011). All forms of energy and material (i.e., heat, gases, radicals, and particles) being exchanged between the ocean and the atmosphere have to pass through the skin layer. The enrichment of naturally occurring surface-active organic compounds modifies the chemical, biological, and physical properties of the skin layer by forming a viscous diffusion layer that retards mass transfer processes.

It has been known for decades that the upper few micrometers of the ocean are generally cooler by several tenths of degree compared to the well-mixed underlying water masses (Saunders, 1967; Schlüssel et al., 1990). Saunders (1967) modeled the heat transfer across the ocean skin layer primarily by molecular conduction, assuming that turbulent motion is suppressed at the air-sea interfacial boundary. Even under calm sea states, small-scaled turbulence causes surface renewal or turbulent eddies to disrupt the ocean skin layer (Jessup et al., 2009; Zappa et al., 1998). Additional cooling occurs due to the combined effect of net

©2018. The Authors.

This is an open access article under the terms of the Creative Commons Attribution-NonCommercial-NoDerivs License, which permits use and distribution in any medium, provided the original work is properly cited, the use is non-commercial and no modifications or adaptations are made.

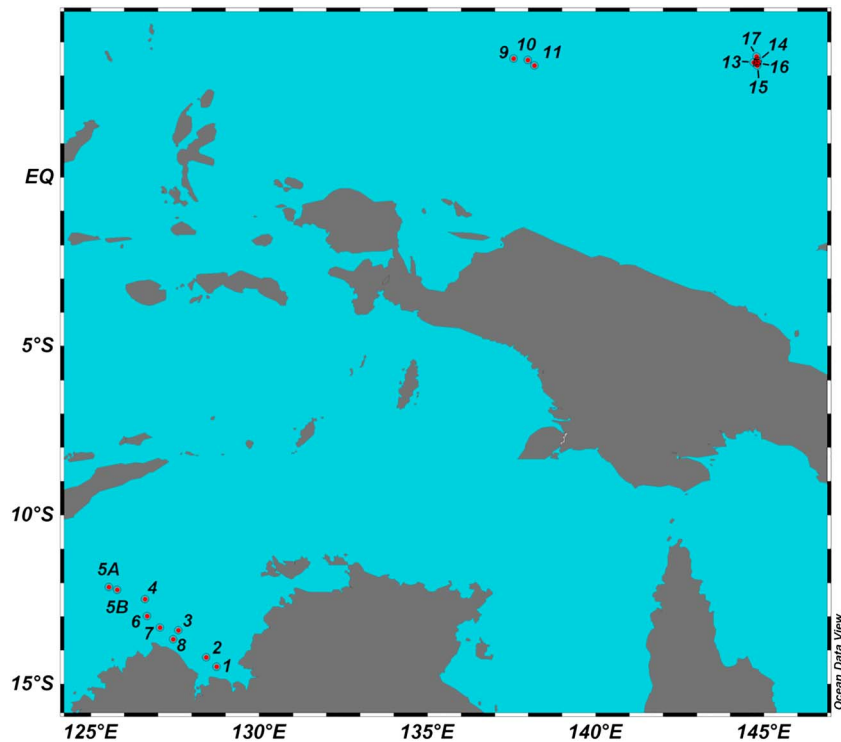


**Figure 1.** Locations of stations for deployment (modified image from Ocean Data View, Schlitzer, 2018).

longwave radiation, evaporation, and the sensible heat flux between the sea surface and the atmosphere (Schlüssel et al., 1997; Yu, 2010). In recent years, attempts have been made to investigate the skin salinity through models (Schlüssel et al., 1997; Song et al., 2015; Yu, 2010; Zhang & Zhang, 2012). Both the temperature and the salinity govern the density (i.e., the stability) of the skin layer. The existence and stability of the skin layer ultimately determines ocean-atmosphere interactions and therefore impacts the hydrologic cycle, ocean circulation, and climate on a global scale (Webster, 1994; Wurl, Ekau, et al., 2017). In addition, two satellite missions have been launched (Lagerloef et al., 2008; Reul et al., 2014) to measure sea surface salinity from space accompanied by large-scale field studies, for example, the Salinity Processes in the Upper Ocean Regional Study (Lindstrom et al., 2015). The satellite measurements detect salinity in the upper centimeters of the ocean based on the microwave brightness temperature at the L band (1.4 GHz). While this sensing depth is deeper than the proposed thickness of the saline boundary layer of 200  $\mu\text{m}$  (Katsaros, 1980), it has been noted that the exponential decay of penetrating radiation energy within the uppermost few centimeters of the ocean's surface makes the satellite-based sensor signal sensitive to changes in the skin salinity (Yu, 2010). However, calibration and validation of satellite-based measurements of salinity is challenging since conventional sampling platforms (e.g., Argo and moored buoys, and research vessels [RVs]) typically measure in situ salinity in the upper 1–5 m of the ocean (Boutin et al., 2016). In addition, Vinogradova and Ponte (2013) reported concerns about variability on short horizontal scales (shorter than the satellite's coverage) contributing to a mismatch between in situ and satellite data. The aim of this study was to determine the prevalence of the saline skin layer in the tropical ocean. We examine time series data from high-resolution in situ measurements on the saline and thermal skin layer with respect to atmospheric forcing, that is, evaporation, precipitation, and wind speed. Finally, we discuss density anomalies and surface renewal.

## 2. Materials and Methods

### 2.1. Study Area

During the expedition Air  $\downarrow$ Sea on the RV *Falkor* (cruise no. FK161010), we occupied 17 stations in the Timor Sea and western Pacific (Figure 1 and Table 1). At Stations 1–3, a faulty setting of the cell constant of the conductivity sensor caused inaccuracy in the calibration and, therefore, in the measurements.

**Table 1**  
Station Number, Bottom Depth, Mixed Layer Depth (MLD), Positions, Date, and Time at Start and End of Deployments

Station	Depth (m)	MLD <sup>a</sup> (m)	Start			End		
			Longitude/Latitude	Date	UTC	Longitude/Latitude	Date	UTC
5A	83	20.3	125.888/−12.222	15 October 2016	23:29	125.923/−12.223	16 October 2016	05:50
5B	76	21.5	125.789/−12.207	17 October 2016	00:33	125.819/−12.201	17 October 2016	06:17
6	76	18.0	125.680/−12.991	17 October 2016	23:18	126.661/−12.960	18 October 2016	05:59
7	89	19.8	127.056/−13.328	19 October 2016	23:15	126.927/−13.319	20 October 2016	06:39
8	82	19.0	127.450/−13.685	19 October 2016	00:20	127.376/−13.642	19 October 2016	02:49
9	4,596	30.8	137.652/3.500	28 October 2016	04:30	137.703/3.484	28 October 2016	06:39
10	4,465	31.1	137.983/3.459	29 October 2016	00:10	138.106/3.406	28 October 2016	06:54
11	4,646	37.4	138.183/3.302	30 October 2016	00:55	138.260/3.254	30 October 2016	05:59
13	4,188	75.6	144.703/3.391	1 November 2016	23:15	144.716/3.411	2 November 2016	06:09
14	4,166	54.2	144.823/3.432	3 November 2016	03:15	144.838/3.430	3 November 2016	06:59
15	4,690	67.4	144.798/3.299	3 November 2016	23:30	144.777/3.340	4 November 2016	04:29
17	4,413	41.7	144.765/3.562	5 November 2016	23:20	144.730/3.621	6 November 2016	06:59

<sup>a</sup>MLD is the depth at which a density change by 0.05 kg/m<sup>3</sup> occurs.

At Station 4, we observed intense cyanobacterial blooms leading to unique sea surface features; this has been reported elsewhere (Wurl et al., 2018). At Station 12, weather conditions did not permit deployment of field equipment (see next section). The salinity data at Station 16 were incorrect, probably due to trapped air bubbles in the flow-through system. For these reasons, no data are reported for Stations 1–4, 12, and 16. Overall, the data sets include 23,743 observations on temperature and salinity anomalies with meteorological forcing, and the data are accessible at the Pangaea repository (Wurl, Mustaffa, et al., 2017).

## 2.2. Measurements of the Skin Layer With a Remote-Controlled Catamaran

We deployed the remote-controlled catamaran Sea Surface Scanner (S<sup>3</sup>; Figure S1 in the supporting information) with an assembly of six glass discs rotating through the sea surface (Ribas-Ribas et al., 2017), where the skin layer adheres to the discs through the phenomenon of surface tension. The adhering skin layer is scraped off on the ascending side of the rotating discs by wipers and pumped through in situ sensors. Rotating glass drum and discs samplers have been shown to effectively collect the skin layer, that is, the sea surface microlayer (Carlson et al., 1988; Shinki et al., 2012). The thickness of the collected skin layer was estimated to be 80 μm based on the disc area, collected volume, and sampling time. The thickness of the collected layers depends on the rotational speed of the discs, salinity, and surfactant concentrations of the skin layer (Shinki et al., 2012) and may have varied during collection. During the operation of S<sup>3</sup> the rotational speed was set to a constant speed of 7.5 rotations per minute. Based on Figure 4 in Shinki et al. (2012), the range of salinity (32.5 to 36.5 practical salinity unit [psu]) in this study could cause a variation in the collected thickness of approximately ±5 μm, whereas the observed surfactant concentrations (49 to 974 μg Teq/L, mean: 127 ± 155 μg Teq/L,  $n = 84$ ) has potentially a greater effect on the thickness with a difference of 18 μm between the minimum and maximum surfactant concentrations (based on equation 6 in Shinki et al., 2012). The wind speed can directly affect the thickness of the collected skin layer, for example, increasing by approximately 10 μm from 3.6 to 7.7 m/s (Figure 2 in Carlson, 1982). Even though the discs are located between the hulls of the catamaran and partially shielded, breaking waves can occasionally splash on the discs and may dilute the skin layer, thereby underestimating the calculated temperature and salinity anomalies. However, 75% of the observed wind speeds were below 7 m/s, and less than 10% of the total number of waves break at 7 m/s (Holthuijsen & Herbers, 1986). At Station 8, we observed the highest wind speeds (maximum of 11.6 m/s) with up to 20% of waves breaking (Holthuijsen & Herbers, 1986), and the calculated anomalies may have been underestimated at Station 8 by occasional splashing on the discs. Based on the following operational details, we estimate a time constant of approximately 7 s for water adhering to the discs to enter the pump tubing, which are protected from direct exposure to solar radiation: (i) the rotational speed of the discs was approximately 8 s per rotation, (ii) the discs were immersed to a depth equivalent to about one third of their diameter (8 s \* 0.66 = 5.3 s), and (iii) the run-off time from the wipers was 2 s, resulting in the time constant of 7 s. The discs are shaded by a low-transmitting dark-colored shield, and their position between the hulls minimizes the warming of the discs and adhering water as well as minimizing

evaporation of the skin samples. Based on observed meteorological conditions and rotational speed of discs, we estimate a maximum bias of 0.04 psu due to evaporation losses from the discs. In addition, continuous immersion prevents warming of the discs. Corresponding underlying water samples were pumped from a depth of 1 m and measured with a second set of in situ sensors. Temperature was measured with a PT1000 with a resolution and accuracy of 0.1 °C (Model MU6100, VWR, Belgium). Conductivity was measured with a two-pole graphite sensor with a resolution of 0.1 mS/cm and accuracy of 0.5% (Model MU6100), as specified by the manufacturer (VWR, Belgium). The salinity was computed from the conductivity according to Gill (1982). Both conductivity sensors, that is, for the skin layer and pumped 1-m bulk water, were calibrated daily and in parallel with the same batch of calibration solution to obtain comparable data. Using the standard reference material P-Series (batch no. P161) from the International Association for the Physical Sciences of the Oceans, we found the accuracy to be better than 0.2% (Table S1). Temperature ( $\Delta T$ ) and salinity ( $\Delta S$ ) anomalies were computed from the difference of temperature ( $T_{S3}$ ) and salinity ( $S_{S3}$ ) in the top 80  $\mu\text{m}$  collected with  $S^3$  and the temperature ( $T_{1\text{m}}$ ) and salinity ( $S_{1\text{m}}$ ) pumped from 1-m depth ( $\pm 0.1$  m), that is,  $\Delta T = T_{S3} - T_{1\text{m}}$  and  $\Delta S = S_{S3} - S_{1\text{m}}$ . In situ data were logged at 0.1 Hz and computed as 1-min averages to obtain more representative skin properties affected by short-scaled processes. Density was computed from salinity and temperature according to Gill (1982). Furthermore,  $\sigma\text{-}t$  is defined as density at a given temperature and salinity minus 1,000  $\text{kg}/\text{m}^3$ . The catamaran  $S^3$  is radio controlled and in this study followed (not tethered) a drifting buoy to support investigations on air-sea gas exchange (to be reported elsewhere). For this reason  $S^3$  moved with the upper surface water masses (at least 1 m in depth) at each station. The distance between the catamaran and the RV *Falkor* was typically  $>100$  m, except for a few minutes at selected stations when it was only a few meters from the ship to compare  $T_{S3}$  with infrared (IR)  $T_{\text{skin}}$  (see Figure 2b). The catamaran has a draft of approximately 0.2 m; that is, the hulls extend 0.2 m into the water. The catamaran  $S^3$  has the capability to collect discrete water samples triggered by the pilot via the remote control. Discrete water samples were analyzed unfiltered for surfactant concentrations using phase-sensitive alternating current voltammetry (Metrohm VA 747, Switzerland) with a hanging mercury drop electrode (Cosović & Vojvodić, 1998). Meteorological data (air temperature, wind speed, wind direction, humidity, and integrated global solar radiation) were collected on the catamaran  $S^3$  at a height of 3 m and on the RV *Falkor* at a height of 11 m. Evaporation rates were computed from a bulk aerodynamic formula (Friehe & Schmitt, 1976).

### 2.3. IR Imagery of Skin Temperature

The skin sea surface temperature (skin SST or  $T_{\text{skin}}$ ) was also determined by an IR camera installed on the upper deck of the RV *Falkor* along with upward- and downward-looking IR radiometers. The IR camera imagery measured thermal radiation from 7.7 to 9.3  $\mu\text{m}$  emitted by the ocean surface (the upper  $\sim 20$   $\mu\text{m}$ ), and  $T_{\text{skin}}$  was obtained with a resolution of 0.02 °C. Calibration with a black body was better than 0.05 °C (Zappa et al., 2012). The difference between the  $T_{\text{skin}}$  and the subskin temperature ( $T_{\text{subskin}}$ ) was calculated directly using the distribution of temperature measured by an IR imager (Jessup et al., 2009).  $T_{\text{skin}}$  was measured by IR imagery at a sampling rate of 100 Hz in 20-min bursts and was measured by IR radiometry at a sampling rate of 1 Hz continuously (both corrected using the upward-looking radiometer for sky reflection; Zappa et al., 1998). High-wavenumber gravity-capillary wave slope was determined by polarimetric imaging from the upper deck of the RV *Falkor* (Zappa et al., 2008, 2012).

In summary,  $S_{S3}$  and  $T_{S3}$  are the salinity and temperature measured in the skin layer collected with  $S^3$  ( $\sim 80$   $\mu\text{m}$  thickness).  $S_{1\text{m}}$  and  $T_{1\text{m}}$  were concurrently measured from 1-m depth directly below the  $S^3$ . The salinity and temperature anomalies are thus defined as  $\Delta S = S_{S3} - S_{1\text{m}}$  and  $\Delta T = T_{S3} - T_{1\text{m}}$ . Temperature in the upper  $\sim 20$   $\mu\text{m}$  was measured with the IR camera ( $T_{\text{skin}}$ ), and its anomaly across the thermal skin layer (approximately the upper 1,000  $\mu\text{m}$ ) is defined as  $\Delta T_{\text{skin}} = T_{\text{skin}} - T_{\text{subskin}}$ . All measurements are illustrated in Figure S2.  $\Delta T$  and  $\Delta T_{\text{skin}}$  are comparable (Figure 2a) considering the different thicknesses of the skin layers (Figure S2) being sampled and the different reference depths for the underlying bulk water. The  $\Delta T_{\text{skin}}$  could not be measured around noon local time due to reflection from direct sun glare. We compared  $T_{\text{skin}}$  and  $T_{S3}$  by navigating  $S^3$  directly under the view of the IR measurements and observed good agreement (Figure 2b). With further distance from the ship, bias between  $T_{\text{skin}}$  and  $T_{S3}$  increased up to 1 °C. Under higher sea state conditions (Figure 2b),  $S^3$  could not safely navigate close to the ship. The larger bias could have originated from the patchiness of the sea surface microlayer thickness within a spatial range of

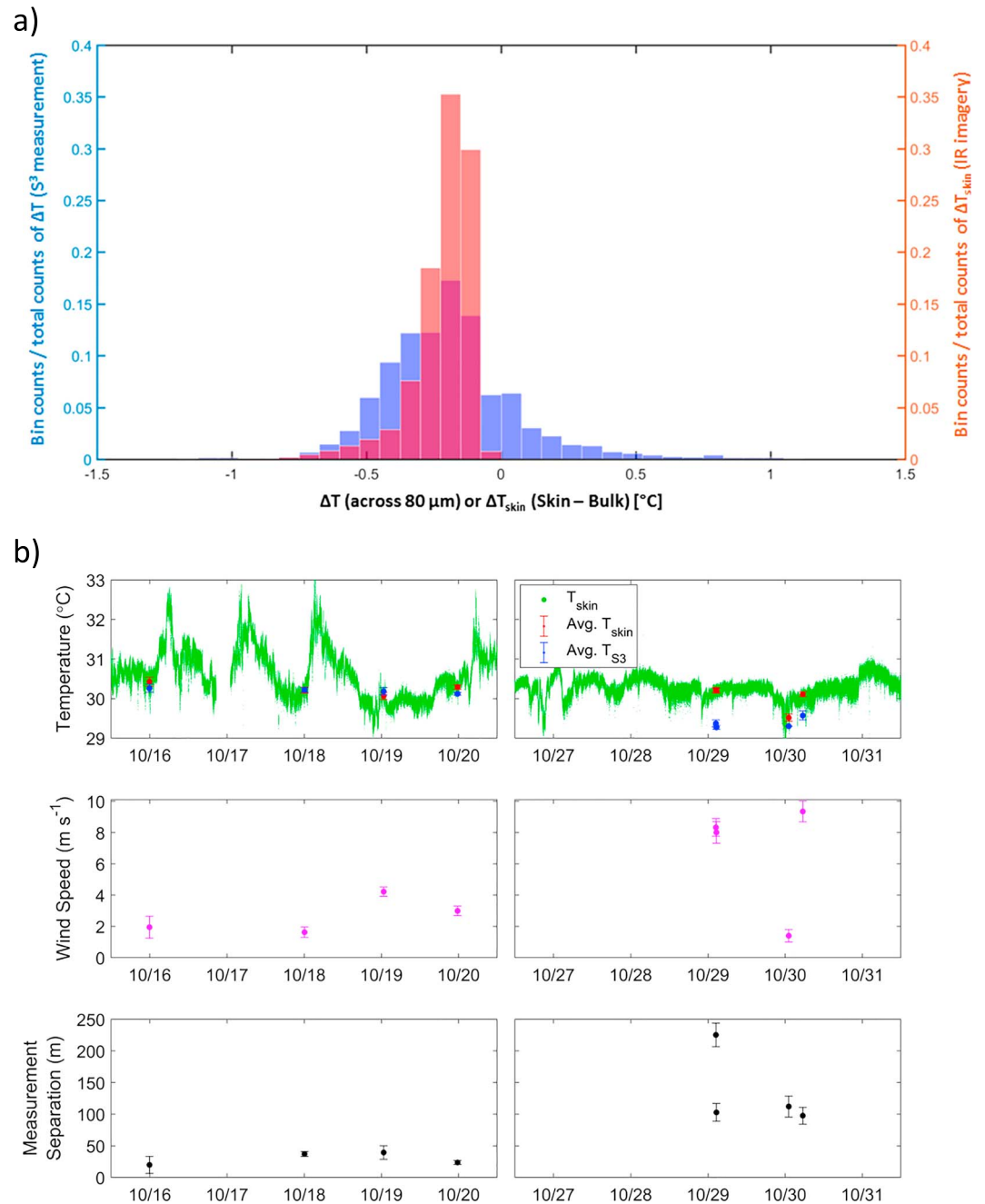


**Figure 2.** (a) Frequency distributions of anomalies (skin-bulk) of the temperature from both the Sea Surface Scanner ( $\Delta T_{S^3}$ ) and infrared (IR) imagery ( $\Delta T_{\text{skin}}$ ) for all experiment periods during which  $S^3$  and IR camera were both operational, typically in the morning. (b) Comparison of  $T_{S^3}$  and  $T_{\text{skin}}$  under the view of the IR measurements (16 to 19 October 2016) and at distances  $>100$  m (28 to 30 October 2016).

50 m (Mustaffa et al., 2017) at wind speeds of up to 6 m/s. Additionally, enhanced evaporative cooling at higher wind speeds above 8 m/s will provide additional bias between  $T_{S^3}$  and  $T_{\text{skin}}$ . The skin layer thickness collected by  $S^3$  (i.e.,  $\sim 80$   $\mu\text{m}$ ) is thicker than the depth layer defined for the IR skin temperature ( $\sim 20$   $\mu\text{m}$ ; Jessup et al., 2009) and potentially approaches the subskin depth. Similar to Ward et al. (2004), we observed that  $T_{\text{subskin}}$  and  $T_{S^3}$  can differ by 0.5 °C (e.g., Station 9, Figure S3) but cover the same temperature range (Station 6), or at least partially (e.g., Station 17). Therefore, quantitative

comparison remains difficult when higher sea states dictated that the sampling locations for  $T_{\text{skin}}$  (in close proximity to the ship) and  $T_{S3}$  were more than 100 m apart.

#### 2.4. Statistical Data Analysis

The statistical analysis was performed with the GraphPad PRISM version 5.0. The analysis of correlation was based on Spearman's correlation test and was considered to be significant when  $p \leq 0.05$ , that is, with a 95% confidence level. Correlation coefficients are reported with 95% confidence intervals (CIs). Rates of increase and decrease of temperature and salinity with precipitation were computed from the time series by regression analysis. Unless otherwise indicated, results are presented as means  $\pm$  standard deviation.

### 3. Results and Discussion

The operational (i.e., apparent) thickness of the skin layer (1–1,000  $\mu\text{m}$ ; Wurl, Ekau, et al., 2017) overlaps with the thickness of the thermal (500–1,000  $\mu\text{m}$ ; Donlon et al., 2002) and saline skin layers (200  $\mu\text{m}$ ; Katsaros, 1980), and the thickness depends on wind speed. The median meteorological conditions at the coastal stations compared with those from the open Pacific were similar (Mann-Whitney test,  $p > 0.08$ ), except for the higher solar radiation at the coastal stations ( $p = 0.0185$ ). Rain events were statistically not compared due to the limited number of observations. From these results, we conclude that no continental effect on the meteorological conditions occurred at Stations 5 to 8. The mixed layer depths (Table 1) at the shallower coastal stations (Stations 5 to 8) varied in a narrow range from 18.0 to 21.5 m, and we conclude that vertical mixing was similar among stations in the coastal regime.

#### 3.1. Thermal Skin Layer

The temperature difference across the skin layer,  $\Delta T_{\text{skin}}$ , is the skin SST minus the subskin SST (Jessup et al., 2009). The skin SST is defined as the radiometric temperature measured across a very small depth of approximately 20  $\mu\text{m}$ . The subskin SST represents the temperature at the base of the thermal skin layer ( $\sim 1,000 \mu\text{m}$  according to the definition in Donlon et al., 2002).  $\Delta T_{\text{skin}}$  measured directly from IR imagery was  $-0.2257 \pm 0.2828 \text{ }^\circ\text{C}$  (median =  $-0.1850 \text{ }^\circ\text{C}$ ), and the histogram (Figure 2a) shows that the skin temperature was always cooler than the water at the base of the skin layer. Temperature ( $\Delta T$ ) and salinity ( $\Delta S$ ) anomalies across the upper 1-m layer were measured with the rotating glass disc sampler mounted on  $S^3$  (Ribas-Ribas et al., 2017) collecting the skin layer with a thickness of 80  $\mu\text{m}$ . The mean difference between the skin temperature from  $S^3$  and the underlying water at 1-m depth was  $\Delta T = -0.19 \pm 0.25 \text{ }^\circ\text{C}$  (median =  $-0.20 \text{ }^\circ\text{C}$ ), and the histogram (Figure 2a) shows that the upper 80- $\mu\text{m}$  layer was cooler 75% of the time compared to the bulk temperature at 1-m depth. Warming of the skin, for example, positive  $\Delta T$ , and directly underlying layers can occur via insolation of the near-surface water during calm sunny days (Murray et al., 2000) as was observed at several stations in our study (Figure 3). Warming occurred at times with strong solar radiation ( $>600 \text{ W/m}^2$ ) and low wind speeds ( $<2 \text{ m/s}$ ), that is, between 00:51 and 02:51 UTC at Station 6 (Figure 4) and between 03:35 and 04:35 UTC at Station 5B (Figure S4) by  $0.4 \text{ }^\circ\text{C}$ . At Station 17, solar radiation declined below  $400 \text{ W/m}^2$  at 05:53 UTC (Figure 4) and  $\Delta T$  stabilized to  $-0.3 \text{ }^\circ\text{C}$  despite very low wind speeds ( $<1 \text{ m/s}$ ). Under such low wind speed conditions, free convection led to constant temperature and salinity, but their anomalies remained. With constant low winds ( $<2 \text{ m/s}$ ) and as solar radiation reached the level of  $600 \text{ W/m}^2$ , the upper 80- $\mu\text{m}$  layer became warmer than the underlying water at Station 6 (Figure 4). However, increasing breezes from  $<2$  to  $4 \text{ m/s}$  (i.e., 04:21 UTC at Station 6, Figure 4, and 01:39 UTC at Station 5B, Figure S4) can cool down the skin by  $0.2\text{--}0.5 \text{ }^\circ\text{C}$  increasing the temperature anomaly  $\Delta T$  and probably cooling the underlying water to some extent.

At Station 7, Figure 5 shows the IR and polarimetric imagery of the ocean's surface before, during, and following a rain event (rain rate:  $47 \text{ mm/hr}$ ; see Figure 4). Prior to the rain event, the IR imagery (Figure 5a) shows the brightness temperature patterns (roughly circular warmer upwelling plumes of  $O(0.1 \text{ m})$ ) suggestive of buoyancy-driven circulation (Zappa et al., 1998) with darker veins of cooler temperature suggesting convergence zones with no apparent structure aligned with the dominant wind direction. Additionally, the polarimetric imagery shows the ocean surface waves to be devoid of capillary waves and only smoother short wind waves in the presence of longer swell. In Figure 5b, the rain is observed as black (cool), very fine circles. As raindrops impact the water surface, small localized light (warm) patches are generated. The warm patches are caused by energetic mixing disrupting the thin, cool skin layer of  $O(1 \text{ mm})$ , and warm water is

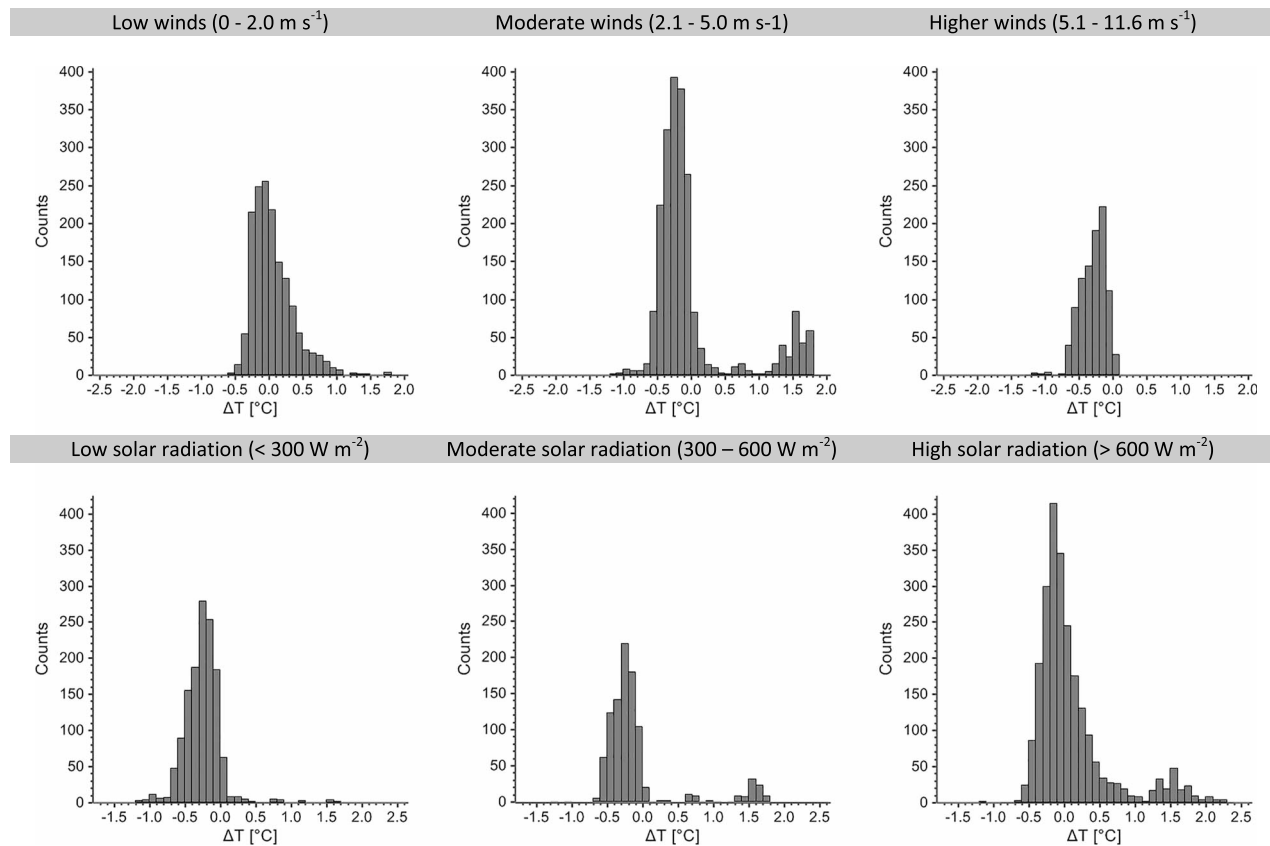


**Figure 3.** Frequency distributions of anomalies (skin-bulk) of the temperature ( $\Delta T$ ) at three regimes of wind speed and solar radiation.

entrained from below. At this point, the background buoyancy-driven circulation is still apparent. Figure 5b demonstrates that the spatial extent of individual raindrops is seen to influence spatial scales of  $O(10\text{ cm})$  or less that will eventually affect the whole ocean surface. This process significantly enhances mixing (Zappa et al., 2009). This scale of  $O(10\text{ cm})$  is comparable to small-scale microbreaking waves (Zappa et al., 2001, 2004). The polarimetric imagery in Figure 5b shows the ocean surface to be dominated by ring waves generated by the impact of the raindrops. The impact of raindrops produces an initial crater that evolves into the ring waves that propagate outward and demonstrate dispersive properties. Following the rain event in Figure 5c, the surface IR temperature shows long cool streaks parallel to the capillary-gravity ocean wind-wave direction seen in the polarimetric imagery suggesting small-scale secondary flows of Langmuir circulation. The streaks in the IR imagery have widths of  $O(0.1\text{--}1\text{ m})$  and are representative of convergence zones set up by the secondary flow.

As shown in Figure 6, the mean  $\Delta T_{\text{skin}}$  across upper  $1,000\text{-}\mu\text{m}$  thermal boundary layer at Station 7 was  $-0.10 \pm 0.02\text{ }^\circ\text{C}$  prior to the rain,  $-0.15 \pm 0.03\text{ }^\circ\text{C}$  during the rain, steadily increasing up to  $-0.6\text{ }^\circ\text{C}$  during the intense rain, and then dropping to  $-0.14 \pm 0.02\text{ }^\circ\text{C}$  following the rain. During this same rain event with an average rain rate of  $47\text{ mm/hr}$ , the thermal skin layer was cooler by  $-1.0\text{ }^\circ\text{C}$  and similar to predicted cooling of  $0.9\text{ }^\circ\text{C}$  at a rain rate of  $40\text{ mm/hr}$  (Figure 4 in Schlüssel et al., 1997) based on surface renewal theory with a renewal time of  $100\text{ s}$ . However, after passing of the rain front, calming winds and increasing solar radiation caused the skin layer to quickly warm up by approximately  $0.05\text{ }^\circ\text{C/min}$  over a time period of  $27\text{ min}$  (03:25 to 03:52 UTC at Station 7, Figure 4), whereas the temperature of the underlying water increased by only  $0.025\text{ }^\circ\text{C/min}$ . After 03:52 UTC, the general trend of warming continued with cyclic cooling by approximately  $0.2\text{ }^\circ\text{C}$  until 05:18 UTC. Before the rain event, the rate of cooling was higher in the skin layer ( $0.17\text{ }^\circ\text{C/min}$ ) than in the underlying water ( $0.08\text{ }^\circ\text{C/min}$ ) and occurred over a period of  $15\text{ min}$  (02:57 to 03:12 UTC). The cooling effect of rain on the skin layer was not effective at lower rain rates ( $<3\text{ mm/hr}$ ) and wind speeds of up to  $6\text{ m/s}$  (Stations 10 and 11 in Figure S4), and a warming by approximately  $0.5\text{ }^\circ\text{C}$  in the skin layer was observed. Overall, our in situ data support conclusions from models (Yu, 2010) and other

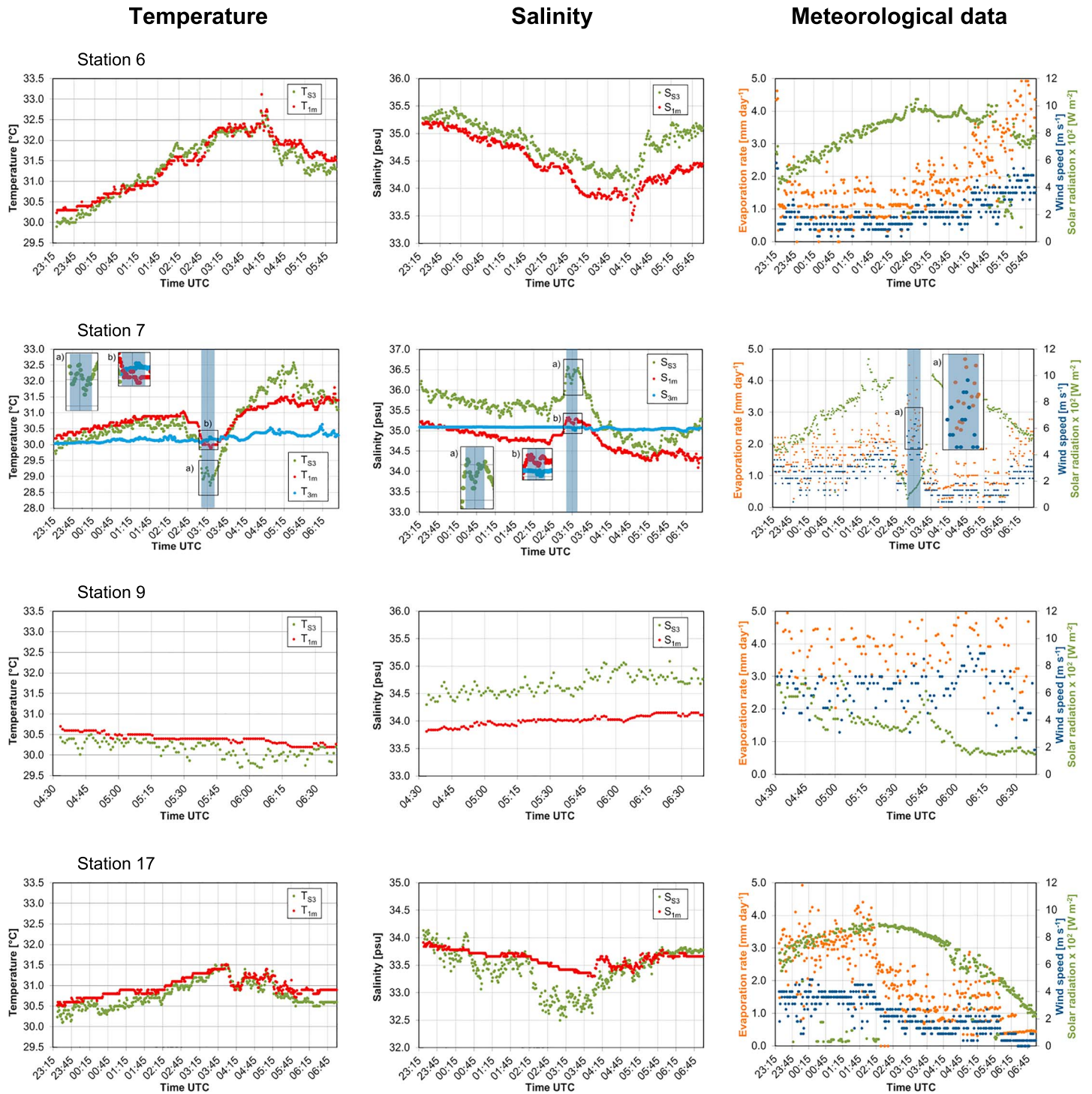


**Figure 4.** Time series of temperature salinity and meteorological data for Stations 6, 7, 9, and 17. Time series of temperature and salinity include the skin (green) and bulk (red) layer. Time series on meteorological data include evaporation rates (orange), wind speed (blue), and solar radiation (green). Blue rectangles in figures for Station 7 indicate a rain event with an average rainfall rate of 47 mm/hr, and blue lines represent ship-based temperature and salinity measurement from 3-m depth. Slightly different timing of rain events presented in this figure and in Figures 4 and 6 is due to different locations of measurements (this figure and Table 2: catamaran S<sup>3</sup>; Figures 4 and 6: RV *Falkor*) and types of rain sensors with different sensitivities.

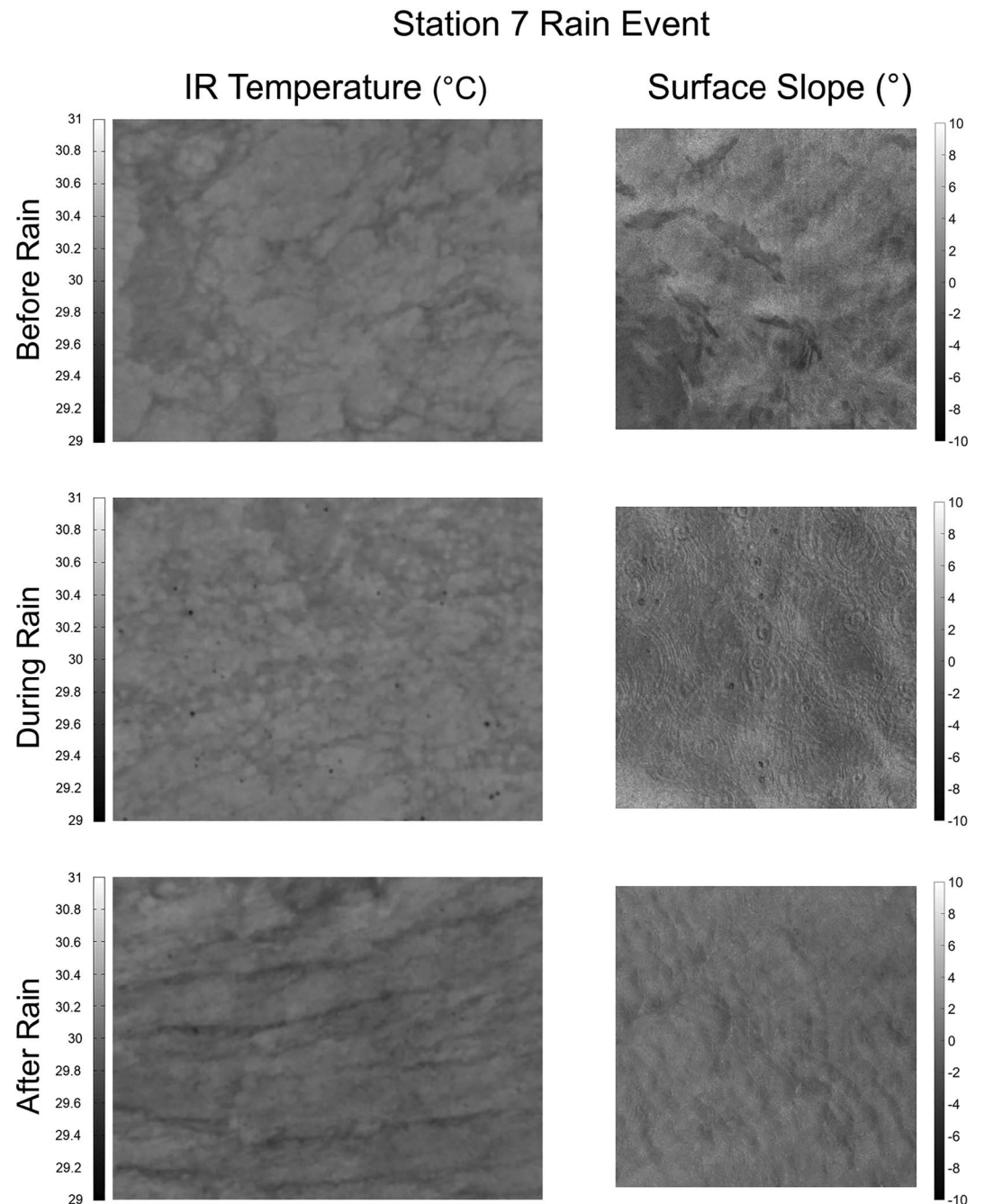


**Figure 5.** Infrared and polarimetric imagery at Station 7 (a) before, (b) during, and (c) following a rain event. Each image has a size of approximately  $1.5 \text{ m} \times 1.5 \text{ m}$ . The wind speeds and UTC times are as follows: “Before Rain” is 3.6 m/s at 02:56:13 UTC; “During Rain” is 3.4 m/s at 02:58 UTC; and “After Rain” is 5.8 m/s at 03:07 UTC. The gray level for the infrared (IR) imagery corresponds to skin sea surface temperature and for the polarimetric imagery corresponds to the ocean surface slope, represented as an angle in degrees from horizontal.

field studies (Asher, Jessup, & Clark, 2014) that very low winds ( $<2 \text{ m/s}$ ) and moderate solar radiation ( $>600 \text{ W/m}^2$ ) will cause the skin layer to warm up and  $\Delta T$  to become positive.

### 3.2. Saline Skin Layer—General Description

Evaporation and precipitation are the major factors contributing to the anomalies of salinity in the near-surface layer (Soloviev & Lukas, 2013), but in opposite directions. Evaporation occurs constantly, provided

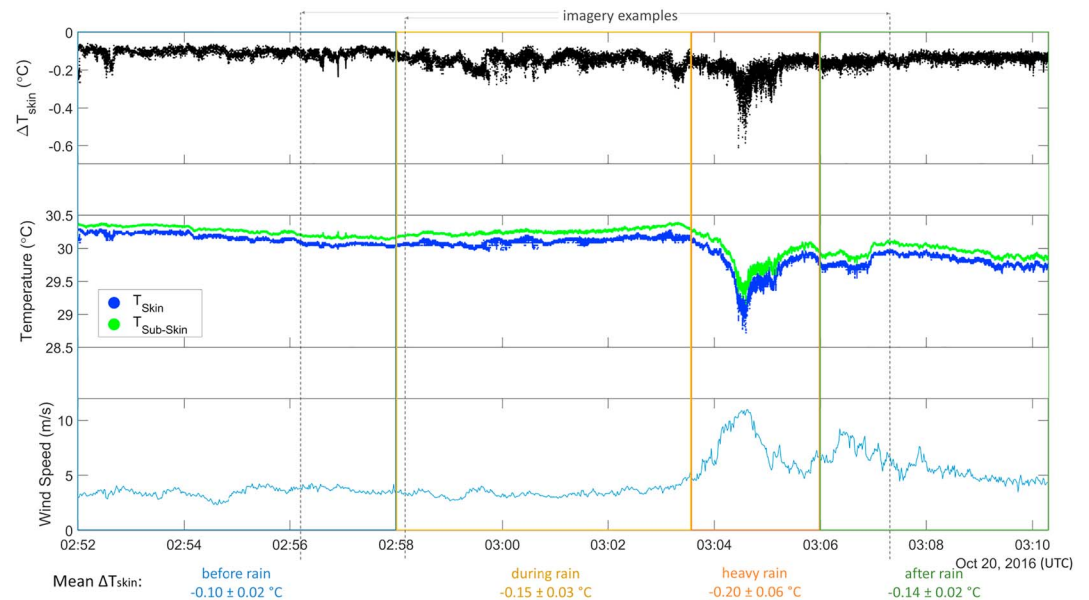


**Figure 6.** Skin sea surface temperature (SST;  $T_{skin}$ ), subskin SST ( $T_{subskin}$ ),  $\Delta T_{skin}$ , and wind speed at Station 7 that follows before a rain event (blue box), during a rain event (yellow box) as it persists to a heavy rain (orange box), and continuing to after the rain event (green box). Slightly different timing of rain events presented in this figure and Table 2 is due to different locations of measurement (this figure: RV *Falkor*; Table 2: catamaran  $S^3$ ) and types of rain sensors with different sensitivities. Dashed lines refer to timing of imagery shown in Figure 5.

the overlying atmosphere is unsaturated, and absorbs latent heat (cooling effect of the skin) and removes water vapor (salting effect of the skin). Precipitation dilutes the salinity of the near-surface layer (discussed in section 3.3) and is restricted by spatial and temporal variations of rainfall events. Our observed salinity anomalies in the skin layer are shown in Figure 7a, and the mean difference of the in situ salinity between the skin and the underlying water was  $\Delta S = 0.40 \pm 0.41$  psu (median = 0.34 psu). Overall, 83% of our observations confirmed the presence of a more saline skin layer, i.e., higher salinity in the skin compared to the underlying water (Figure 7a). These observations are generally in agreement with models from the literature, but our reported  $\Delta S$  is higher compared to modeled anomalies (0.15 psu, Yu, 2010; 0.25 psu, Zhang & Zhang, 2012; and 0.15 psu, Song et al., 2015). This can perhaps be explained by differences between our sampling methodology (simultaneous skin and underlying water sampling) and those used for the modeled anomalies, for example, modeled only for the night (Zhang & Zhang, 2012) or referring to a different reference depth (Song et al., 2015). Multiple peaks in the frequency distribution of the whole data set originate from specific anomalies at the different stations, and not from concurrent meteorological events, that is, rain and upcoming winds inducing vertical mixing (Figures 7 and S5). The majority of negative  $\Delta S$ , i.e., a less saline skin layer, occurred at Station 17 between 00:40 and 05:15 UTC (Figure 4), perhaps due to the presence of a freshwater lens caused by a nonlocal rain event. Such freshwater lenses spread horizontally and can persist for hours to days under conditions of weak winds, high solar radiation (for stable stratification) as encountered at Station 17 (Figure 4), or prolonged precipitation events (Bellenger et al., 2017; Soloviev et al., 2015). Consequently, fresh water lenses can potentially merge to form large and very warm pools under calm sea conditions. Surfactant films have been suggested to modify salinity anomalies ( $\Delta S$ ; Yu, 2010) and recently shown by Wurl et al. (2018) in the presence of surface slicks. However, in this study  $\Delta S$  correlated weakly with the concentrations of surfactants in the skin layer ( $r = 0.266$ , 95% CI [0.089, 0.428],  $n = 83$ ) but shows that surfactant concentrations as Triton-X100 equivalent ( $Teq$ ) below 100  $\mu g$   $Teq/L$  has no effect on  $\Delta S$  (Figure S7). Conclusive statements about inhibition of salinization at increasing concentrations of surface-active substances, as observed at Station 4 (reported by Wurl et al., 2018), cannot be made due to the limited number of observations in the presence of higher concentrations.

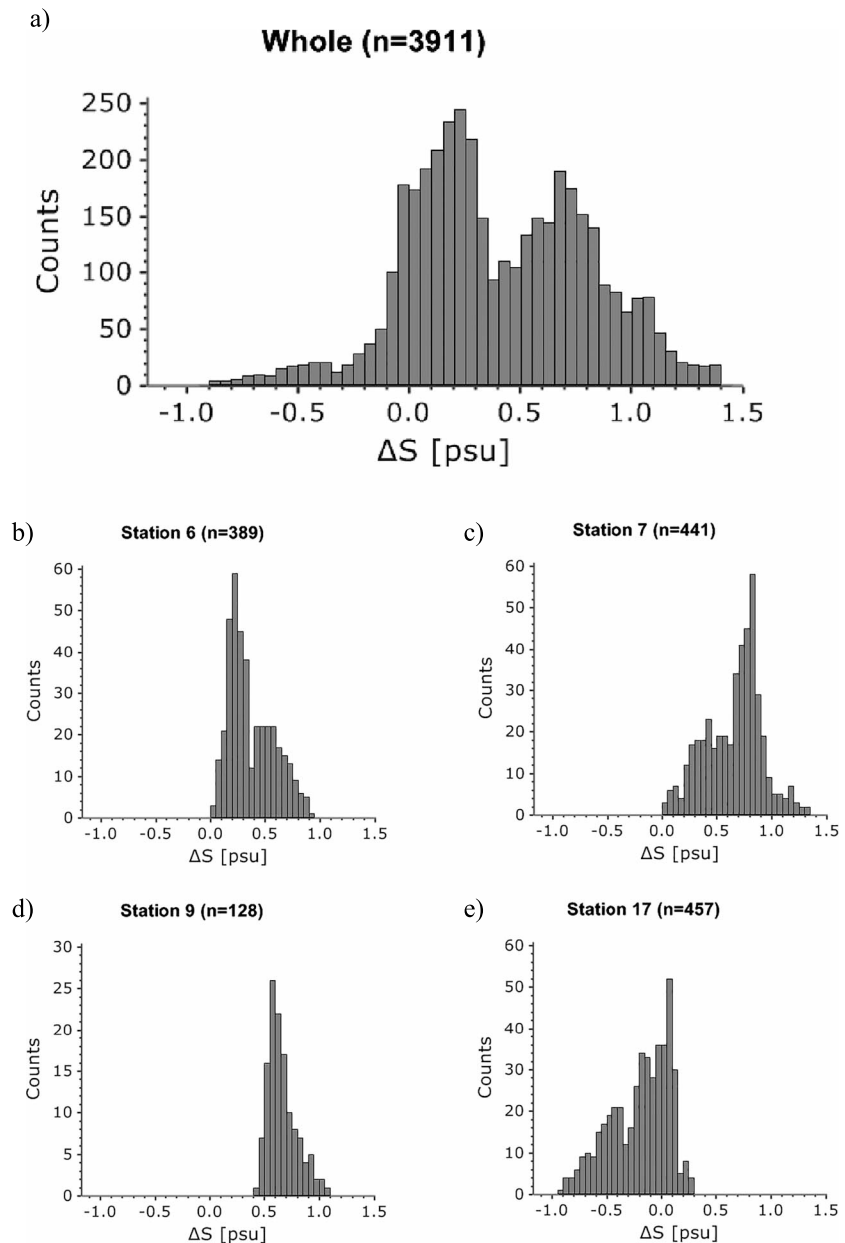


**Figure 7.** Frequency distributions of anomalies (skin-bulk) of the salinity ( $\Delta S$ ) from the (a) whole data set and (b–e) selected stations obtained with the Sea Surface Scanner. Frequency distributions from other stations are shown in Figure S5.

### 3.3. Saline Skin Layer at Rainy Conditions

At Station 7 (Figure 4), rainfall rates between 7.4 and 105 mm/hr (mean  $\pm$  standard deviation =  $47 \pm 32$  mm/hr) caused a salinity decrease in the skin layer and underlying water (averaged  $-0.6$  and  $-0.4$  psu, respectively) after the rainfall. It is intuitive to expect a freshening of the near-surface layer of the ocean during and after rain events, and this has been reported in the literature (Asher, Jessup, Branch, & Clark, 2014; Boutin et al., 2013; Reverdin et al., 2012; Soloviev & Lukas, 2013) for depths of 0.1 m and below. Our observations show that  $S_{S3}$  was 35.69 psu ( $\pm 0.17$  psu,  $n = 1368$ ), 36.38 psu ( $\pm 0.12$  psu,  $n = 97$ ), and 35.03 psu ( $\pm 0.48$  psu,  $n = 1188$ ) before, during, and after the rain event, respectively. The bulk salinity ( $S_{1m}$ ) was 34.92 psu ( $\pm 0.14$  psu,  $n = 1368$ ), 35.24 psu ( $\pm 0.06$  psu,  $n = 97$ ), and 34.56 psu ( $\pm 0.28$  psu,  $n = 1188$ )

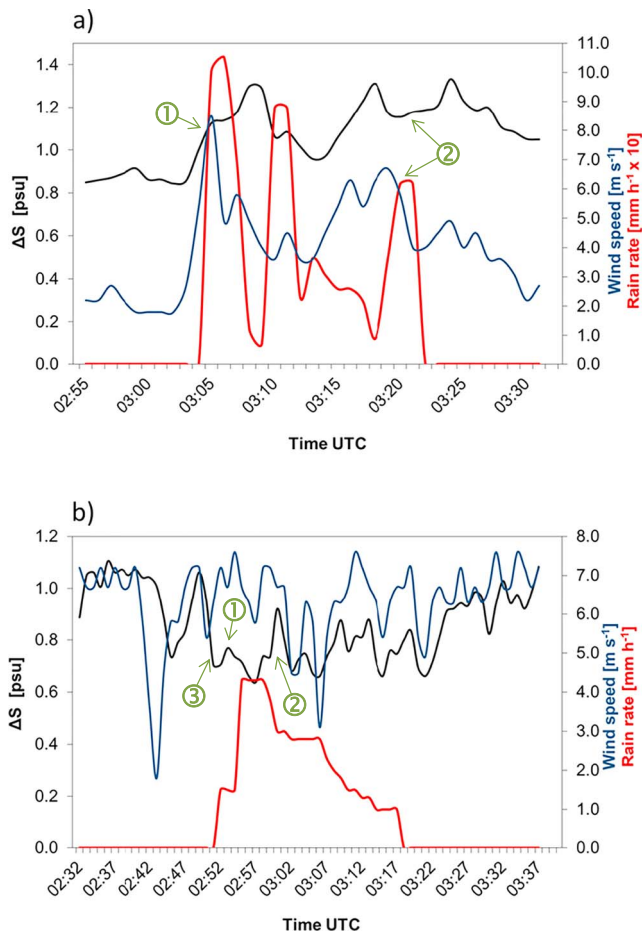


**Figure 8.** Time series of salinity anomaly ( $\Delta S$ ), wind speed, and rain rate at (a) Station 7 and (b) Station 10.

before, during, and after the rain event, respectively. Variability in the salinity was greater in the skin than in the bulk water as expected due to the immediate effects of the high evaporation rates.  $T_{S3}$  was  $30.41\text{ }^{\circ}\text{C}$  ( $\pm 0.26\text{ }^{\circ}\text{C}$ ,  $n = 1368$ ) before the rain, cooled down to  $29.03\text{ }^{\circ}\text{C}$  ( $\pm 0.17\text{ }^{\circ}\text{C}$ ,  $n = 97$ ) due to the rainfall, but then warmed up to  $31.34\text{ }^{\circ}\text{C}$  ( $0.84\text{ }^{\circ}\text{C}$ ,  $n = 1188$ ), that is, was warmer compared to the initial  $T_{S3}$  before the rain. Similarly, initial  $T_{1m}$  warmed up from  $30.66\text{ }^{\circ}\text{C}$  ( $\pm 0.22\text{ }^{\circ}\text{C}$ ,  $n = 1368$ ) to  $31.08\text{ }^{\circ}\text{C}$  ( $\pm 0.42\text{ }^{\circ}\text{C}$ ,  $n = 1188$ ) with an intermittent cooling during the rain to  $30.03\text{ }^{\circ}\text{C}$  ( $\pm 0.08\text{ }^{\circ}\text{C}$ ,  $n = 97$ ). Before the rainfall event, we observed a salinity anomaly of  $\Delta S = +0.77\text{ psu}$ . After the rainfall event, we observed a salinity anomaly of  $\Delta S = +0.47\text{ psu}$ , that is, a relative freshening similar to what has been reported in the literature (Asher, Jessup, Branch, & Clark, 2014). Counterintuitively, during the rain event the salinity in the skin layer and the underlying water increased by 0.69 and 0.32 psu, respectively. This generated an increase in the salinity anomaly in the skin layer, although it was temporary. The increase in salinity during the rain event is presumably caused by vertical mixing due to wind speeds of  $>8\text{ m/s}$  and a salinity of approximately 35.07 psu at 5 m (obtained from the concurrent deployment of conductivity, temperature and depth sensors from 02:59 to 03:18 UTC, Figure S6). After the rainfall event, the wind speed dropped to below 2 m/s, allowing the salty surface layer to sink, and continuing drizzling (i.e., at rain rates below detection of 0.25 mm/hr) and horizontal advection of freshwater lenses located in proximity of sampling may have led to the observed freshening. However, detailed analysis of this event is limited as data at further depths are not available and freshening is a complex process (Schlüssel et al., 1997). Freshening of the near-surface layer (0.11 m depth; Asher, Jessup, Branch, & Clark, 2014) was reported during rain events even at lower rain rates (maximum at 20 mm/hr), but in their observations (Figure 6 in Asher, Jessup, Branch, & Clark, 2014) the wind dropped from 9 to  $<3\text{ m/s}$  as the rain event occurred, indicating that vertical mixing rates should have declined. In our observations, the larger increase of salinity in the skin layer compared

to the underlying water (0.69 versus 0.32 psu) implies continuing evaporation of water from the skin layer. Indeed, evaporation rates, derived from a bulk aerodynamic formula (Friehe & Schmitt, 1976), were highest during the heavy rainfall events at Station 7 (Figure 2) and Station 8 (Figure S4). Higher evaporation rates during the rain were accompanied by a decrease of the relative humidity at 3 m ( $S^3$ ) and 11.9 m (ship-based) by 1.7% (down to 80.4%) and 3.1% (down to 77.1%), respectively. Similarly, the air temperature dropped by  $1.4\text{ }^{\circ}\text{C}$  (down to  $27.5\text{ }^{\circ}\text{C}$ ) and by  $1.7\text{ }^{\circ}\text{C}$  (down to  $26.7\text{ }^{\circ}\text{C}$ ), respectively. An average evaporation rate of 4 mm/day alone causes a salinity increase of 1.2 psu/min in the skin layer at Station 7, but from our high-resolution measurements at Station 7, we can conclude that salinity increased at a rate of 0.09 and 0.05 psu/min in the skin layer and underlying water, respectively, with the onset of rainfall. That means the additional salinity of 1.2 psu/min needs to be diluted by a factor of 13 to match the observation, or  $60\text{ ml}\cdot\text{min}^{-1}\cdot\text{m}^{-2}$  ( $= 1/13$  of 47-mm/hr rain rate or equally  $1/13$  of  $780\text{ ml}\cdot\text{min}^{-1}\cdot\text{m}^{-2}$ ) needs to remain in the skin to match observation. Of the total rain rate, 7.7% is represented by  $60\text{ ml}\cdot\text{min}^{-1}\cdot\text{m}^{-2}$ , that is,  $780\text{ ml}\cdot\text{min}^{-1}\cdot\text{m}^{-2}$ . Our approach is simplified but matches a theoretical approach by Schlüssel et al. (1997) estimating this fraction to be 5% for a rain rate of 50 mm/hr. The majority of the rainwater (i.e., 92% to 95% of  $780\text{ ml}\cdot\text{min}^{-1}\cdot\text{m}^{-2}$ ) submerged under the skin into the water column. The dilution of 1,000 L of underlying bulk water (1 m depth with  $1\text{ m}^2$  surface area) caused the salinity of 34.89 psu (Station 7 between 02:46 s and 02:55 UTC, Figure 2) to drop by 0.035 psu. This drop of salinity is compensated by vertical mixing with more saline water from depths below 5 m based on the profile of conductivity and temperature measurements (Figure S6).

After the rainfall event, salinity decreased with a rate of  $-0.04$  and  $-0.02\text{ psu/min}$  in the skin layer and underlying water, respectively, compared to rates of increase with the onset of rain of 0.09 and 0.05 psu/min. It

**Table 2**  
Meteorological Records at Each Station

Station	<i>n</i>	Air temperature (°C)	Humidity (%)	Wind (m/s)	Evaporation rate (mm/day)	Solar radiation (W/m <sup>2</sup> )		
						min	max	
5A	381	29.5 ± 0.2	68.0 ± 1.2	1.7 ± 0.9	2.1 ± 1.0	761 ± 187	63	918
5B	345	29.7 ± 0.2	68.5 ± 1.2	1.6 ± 0.8	2.3 ± 1.1	756 ± 235	107	1,039
6	335	29.2 ± 0.2	75.0 ± 1.2	1.7 ± 0.4	2.3 ± 1.5	792 ± 181	211	1,049
7	444	28.9 ± 0.7	80.3 ± 2.7	2.3 ± 1.3	1.7 ± 0.9	645 ± 251	62	1,123
8	150	27.3 ± 1.5	85.7 ± 4.0	7.0 ± 3.0	4.4 ± 1.5	387 ± 258	25	988
9	130	28.7 ± 0.1	83.5 ± 1.5	6.3 ± 1.4	4.7 ± 0.9	361 ± 164	141	724
10	405	27.6 ± 0.5	88.1 ± 2.0	6.1 ± 1.4	3.4 ± 0.9	136 ± 24	39	185
11	305	27.4 ± 0.3	88.0 ± 1.0	4.4 ± 2.1	2.5 ± 1.2	194 ± 74	83	402
13	414	29.6 ± 0.3	80.6 ± 2.5	5.0 ± 1.1	4.3 ± 0.9	475 ± 196	109	872
14	225	28.7 ± 0.4	86.1 ± 2.1	3.0 ± 1.0	1.8 ± 0.8	298 ± 186	63	828
15	299	30.2 ± 0.1	78.9 ± 1.6	4.9 ± 0.7	4.5 ± 0.7	534 ± 253	105	942
17	459	30.3 ± 0.5	74.0 ± 2.2	2.2 ± 1.3	2.4 ± 1.4	606 ± 274	30	933
Rain event								
Station	<i>n</i>	Start UTC	End UTC	Wind (m/s)	Rain rate (mm/hr)			
7	17	03:05	03:22	5.2 ± 1.3	47 ± 32			
8	22	01:39	02:01	9.3 ± 1.0	94 ± 232			
10	25	02:52	03:17	6.1 ± 1.1	2.9 ± 1.0			
11	11	00:57	01:08	1.3 ± 0.7	1.7 ± 0.6			
11	19	04:11	04:30	6.1 ± 0.6	1.2 ± 0.2			

Note. Values given as average ± 1 standard deviation, minimum (min), and maximum (max) values.

implies that salting by evaporation and vertical mixing is twofold faster than freshening by dilution with rainwater ( $S_{\text{Rain}} = 0.002$  psu; derived from chloride concentrations) in rainwater samples. At Station 8, we observed similar increases of salinity in the skin layer (0.8 psu) and bulk water (0.5 psu) with the onset of higher wind speeds (from 4.9 to 9.8 m/s at 01:18 UTC; Figure S4). However, the rain event (mean rain rate 290 mm/hr) occurred 20 min after the observation of increased salinity, further supporting wind and vertical mixing as factors to increase salinity at the sea surface. Furthermore, our data in Figure 8 demonstrate that anomalies in salinity generally follow the wind speed rather than the rain rates. For example, small peaks in  $\Delta S$  remain in the observations aligned with peaks in the wind speed (i.e., event ① in Figure 8a and events ① and ②; in Figure 8b), meaning that the skin layer is stirred up by breezes easily as already discussed above for the cooling effect at Station 6. Our observations are supported by an earlier report (Cronin & McPhaden, 1999) that vertical mixing during rain events, or before such events (i.e., at Station 8), can bring saltier water from the mixed layer to the sea surface and overcome the freshening effect. However, at lower rain rates a drop in  $\Delta S$  was observed due to freshening of the skin layer only (event ③ in Figure 8b) as light rain has insufficient momentum to break through the skin layer (Katsaros & Buettner, 1969; Schlüssel et al., 1997). At high rain rates, a drop in  $\Delta S$  is only observed with a concurrent decrease in wind speed, that is, less vertical mixing and reducing evaporation rates (event ②; in Figure 8a). However, at Station 8 slight freshening occurred during rain events even at high wind speeds (10 to 12 m/s), and in this case the extreme rainfall rates of 290 mm/hr (occasionally up to 700 mm/hr) probably overcame the vertical mixing. In conclusion, the freshening or salting of the skin layer depends on the rates of the counteracting processes of vertical mixing (driven by wind speed) and precipitation (driven by the rain rate). At low rain rates (< 3 mm/hr) and wind speeds below 8 m/s, we observed an immediate freshening of up to 0.25 psu, which diminished after the rain events (Stations 10 and 11, Figure S4) lasting for less than half an hour (Table 2).

### 3.4. Density Anomalies

Our observed densities in the skin layer (Figure 9) confirm its dynamic nature as described through surface renewal models. In comparison, bulk density at 1-m depth is less influenced by atmospheric forcing (i.e., heat flux, evaporation, and wind) and is not showing the cyclic pattern as the skin density. For example,

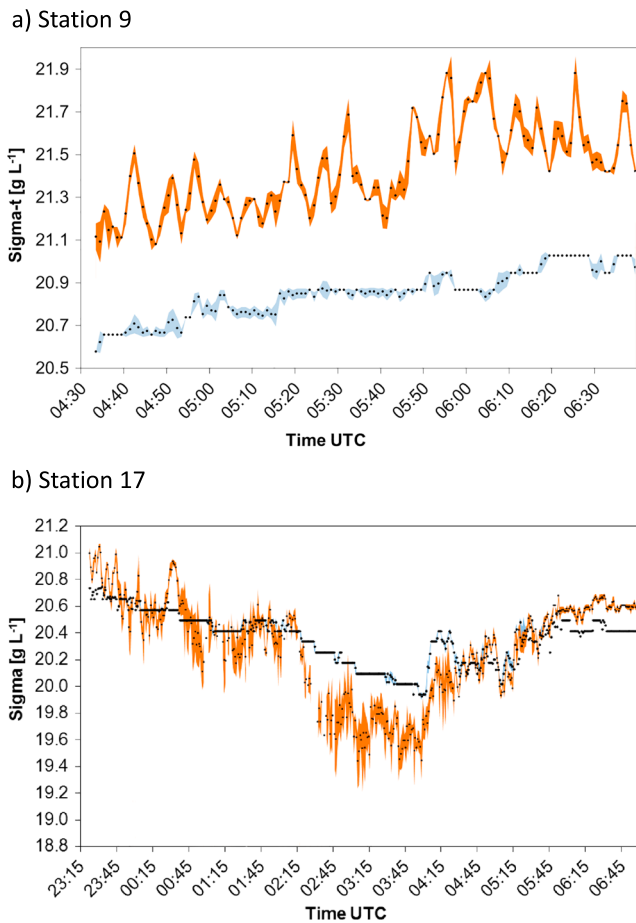


**Figure 9.** Time series of sigma- $t$  densities in the skin (orange) and bulk (blue) at (a) Station 9 and (b) Station 17. Sigma- $t$  is defined as density at given temperature and salinity minus  $1,000 \text{ kg/m}^3$ . Black dots are 1-min average data, and colored bands represent the standard deviation.

at Station 17 the wind calms down close to zero at 06:00 UTC (Figure 2), and at the same time the variance of the skin density reduces to a minimum. The skin layer at Station 9 is regularly mixed with water adjacent to the skin layer. However, due to its thinness, the influence of net heat flux and evaporation increased the density of the skin layer within minutes. The interfacial tension between the skin and adjacent underlying layer can modify the time scale of their mixing and allow the formation of a denser skin atop the underlying water. Despite significant differences between fluid dynamics in the open ocean compared to laboratory tank experiments, the principle of the phenomena of floating denser fluids is supported by laboratory measurements and theoretical modeling showing that denser water can float atop less dense oil (Phan, 2014; Phan et al., 2012) and denser particles can remain suspended on water surfaces (Singh & Joseph, 2005) in the presence of sufficient interface tension. Singh and Joseph (2005) wrote (page 34), “Obviously, a prismatic particle which is denser than the liquid below can float only if the vertical component of interfacial tension is sufficiently large to balance its buoyant weight and will sink when this is no longer true,” and, despite different scales and geometry, we suggest a similar process may occur between the skin and the underlying layer. While we did not make surface tension measurements in this study, Barger et al. (1974) and Antonow’s rule (Adamson, 1976) show that the interfacial tension between the skin layer and underlying water can vary between 0.3 and 1.6 mN/m, thus allowing for the possibility of dense fluid atop less dense fluid. It has been also reported that the skin layer contains hydrophobic material, like dissolved fatty acids (Brinis et al., 2004), surfactants (Wurl et al., 2011) but perhaps sufficiently low to sustain interfacial tension and interfacial tension to prevent the immediate sinking of the denser skin at Station 9 (Figure 9). Indeed, in the Timor Sea (Stations 5B–8) and western Pacific (Stations 10, 11, 13–15, and 17; no data for Station 9) the average concentrations of surface-active substances were  $141 \pm 65 \mu\text{g Teq/L}$  ( $n = 38$ ) and  $101 \pm 68 \mu\text{g Teq/L}$  ( $n = 53$ ), respectively. Those concentrations are low compared to levels for other oligotrophic regions ( $320 \pm 65 \mu\text{g Teq/L}$ ,  $n = 38$ ; Wurl et al., 2011). The interfacial tension could hold the denser

skin layer afloat up to a density anomaly threshold ( $\Delta\sigma_{\text{Threshold}}$ ) of 1.3 g/L (Figure S8). In this study, we did not find a strong correlation between density anomalies and concentrations of surface-active substances ( $r = 0.244$ , 95% CI [0.072, 0.403],  $n = 89$ ); thus, the explanation for finding a denser skin layer remains unclear and will require further research.

#### 4. Conclusions

Results from this study confirm the ubiquitous presence of a saline skin layer in the Indo-Pacific Ocean. The positive salinity anomaly between the skin layer and underlying bulk water persists even in the presence of strong tropical rainfalls. We conclude that evaporation and wind-driven mixing can overcome the freshening of the sea surface by rainwater under moderate wind speeds. During low rainfall rates ( $<3 \text{ mm/hr}$ ), we observed an immediate freshening with the onset of precipitation that disappeared as soon as the rain front passed. Clearly, freshening of the skin, and probably the near-surface layer, is complex and depends on rain rates forcing penetration depths, the amount of introduced freshwater, and the wind speed during and after the rain event. Consequently, future assessment of oceanic rainfall events from satellite surface salinity requires a mechanistic understanding of the fate of freshwater fluxes into the ocean. Such assessment requires more observational platforms (i.e., drifting buoys) and autonomous technology to record skin salinity anomalies similar to what we have done with the catamaran S<sup>3</sup>. Our observations revealed that a denser skin layer can float on less dense bulk water to a certain threshold (in our study:  $\Delta\sigma_{\text{Threshold}} = 1.3 \text{ g/L}$ ), probably due to the presence of sufficient interfacial tension. With our observations, we conclude that interfacial

surface tension exerts a significant control on surface skin renewal rates, a key process in air-sea exchange of gases, heat, and particles. To what extent this new phenomenon affects air-sea interactions on a global scale remains to be answered in future assessments.

**Acknowledgments**

O. W. acknowledges funding by the European Research Council (ERC) project (grant number GA336408). W. M. L. acknowledges logistical support from the Scientific Committee on Ocean Research (SCOR). C. J. Z. acknowledges funding by the Schmidt Ocean Institute (contract number AABM9767). All authors thank the Schmidt Ocean Institute for providing their RV *Falkor* for the expedition AIR ↑SEA (cruise no. FK161010). The captain, officers, and crew of the RV *Falkor* and the science team of FK161010 are acknowledged for their invaluable support during the expedition. Cruise track and S<sup>3</sup> catamaran data of FK161010 are archived at the PANGAEA data publisher (Wurl, Mustafa, et al., 2017). C. J. Z. archives IR and polarimetric data products on Columbia Academic Commons (<https://academiccommons.columbia.edu/>), and raw imagery is available upon request. This is Lamont-Doherty Earth Observatory contribution number 8275. The authors declare no competing financial interests.

**References**

Adamson, A. W. (1976). *Physical chemistry of surfaces*. New York, NY: John Wiley & Sons Inc.

Asher, W. E., Jessup, A. T., Branch, R., & Clark, D. (2014). Observations of rain-induced near-surface salinity anomalies. *Journal of Geophysical Research: Oceans*, *119*, 5483–5500. <https://doi.org/10.1002/2014JC009954>

Asher, W. E., Jessup, A. T., & Clark, D. (2014). Stable near-surface ocean salinity stratifications due to evaporation observed during STRASSE. *Journal of Geophysical Research: Oceans*, *119*, 3219–3233. <https://doi.org/10.1002/2014JC009808>

Barger, W. R., Daniel, W. H., & Garrett, W. D. (1974). Surface chemical properties of banded sea slicks. *Deep Sea Research and Oceanographic Abstracts*, *21*(1), 83–89. [https://doi.org/10.1016/0011-7471\(74\)90022-9](https://doi.org/10.1016/0011-7471(74)90022-9)

Bellenger, H., Drushka, K., Asher, W., Reverdin, G., Katsumata, M., & Watanabe, M. (2017). Extension of the prognostic model of sea surface temperature to rain-induced cool and fresh lenses. *Journal of Geophysical Research: Oceans*, *122*, 484–507. <https://doi.org/10.1002/2016JC012429>

Boutin, J., Chao, Y., Asher, W. E., Delcroix, T., Drucker, R., Drushka, K., et al. (2016). Satellite and in situ salinity: Understanding near-surface stratification and subfootprint variability. *Bulletin of the American Meteorological Society*, *97*(8), 1391–1407. <https://doi.org/10.1175/BAMS-D-15-00032.1>

Boutin, J., Martin, N., Reverdin, G., Yin, X., & Gaillard, F. (2013). Sea surface freshening inferred from SMOS and ARGO salinity: Impact of rain. *Ocean Science*, *9*(1), 183–192. <https://doi.org/10.5194/os-9-183-2013>

Brinis, A., Méjanelle, L., Momzikoff, A., Gondry, G., Fillaux, J., Point, V., & Saliot, A. (2004). Phospholipid ester-linked fatty acids composition of size-fractionated particles at the top ocean surface. *Organic Geochemistry*, *35*(11–12), 1275–1287. <https://doi.org/10.1016/j.orggeochem.2004.04.009>

Carlson, D. J. (1982). A field evaluation of plate and screen microlayer sampling techniques. *Marine Chemistry*, *11*, 189–208.

Carlson, D. J., Cantey, J. L., & Cullen, J. J. (1988). Description of and results from a new surface microlayer sampling device. *Deep Sea Research Part A. Oceanographic Research Papers*, *35*(7), 1205–1213. [https://doi.org/10.1016/0198-0149\(88\)90011-8](https://doi.org/10.1016/0198-0149(88)90011-8)

Ćosović, B., & Vojvodić, V. (1998). Voltammetric analysis of surface active substances in natural seawater. *Electroanalysis*, *10*(6), 429–434. [https://doi.org/10.1002/\(SICI\)1521-4109\(199805\)10:6<429::AID-ELAN429>3.0.CO;2-7](https://doi.org/10.1002/(SICI)1521-4109(199805)10:6<429::AID-ELAN429>3.0.CO;2-7)

Cronin, M. F., & McPhaden, M. J. (1999). Diurnal cycle of rainfall and surface salinity in the western Pacific warm pool. *Geophysical Research Letters*, *26*(23), 3465–3468. <https://doi.org/10.1029/1999GL010504>

Donlon, C. J., Minnett, P. J., Gentemann, C., Nightingale, T. J., Barton, I. J., Ward, B., & Murray, M. J. (2002). Toward improved validation of satellite sea surface skin temperature measurements for climate research. *Journal of Climate*, *15*(4), 353–369. [https://doi.org/10.1175/1520-0442\(2002\)015<0353:TIVOSS>2.0.CO;2](https://doi.org/10.1175/1520-0442(2002)015<0353:TIVOSS>2.0.CO;2)

Friehe, C. A., & Schmitt, K. F. (1976). Parameterization of air-sea interface fluxes of sensible heat and moisture by the bulk aerodynamic formulas. *Journal of Physical Oceanography*, *6*(6), 801–809. [https://doi.org/10.1175/1520-0485\(1976\)006<0801:POASIF>2.0.CO;2](https://doi.org/10.1175/1520-0485(1976)006<0801:POASIF>2.0.CO;2)

Gill, A. E. (1982). *Atmosphere-ocean dynamics*. San Diego, CA: Academic Press.

Holthuijsen, L. H., & Herbers, T. H. C. (1986). Statistics on breaking waves observed as whitecaps in the open ocean. *Physical Oceanography*, *16*(2), 290–297. [https://doi.org/10.1175/1520-0485\(1986\)016<0290:SOBWOA>2.0.CO;2](https://doi.org/10.1175/1520-0485(1986)016<0290:SOBWOA>2.0.CO;2)

Hunter, K. A. (2005). Chemistry of the sea-surface microlayer. In P. S. Liss, & R. A. Duce (Eds.), *Sea surface and global change* (chap. 9, pp. 287–319). UK: Cambridge University Press.

Jessup, A. T., Asher, W. E., Atmane, M., Phadnis, K., Zappa, C. J., & Loewen, M. R. (2009). Evidence for complete and partial surface renewal at an air-water interface. *Geophysical Research Letters*, *36*, L16601. <https://doi.org/10.1029/2009GL038986>

Katsaros, K., & Buettner, K. J. (1969). Influence of rainfall on temperature and salinity of the ocean surface. *Journal of Applied Meteorology*, *8*(1), 15–18. [https://doi.org/10.1175/1520-0450\(1969\)008<0015:TOROTA>2.0.CO;2](https://doi.org/10.1175/1520-0450(1969)008<0015:TOROTA>2.0.CO;2)

Katsaros, K. B. (1980). The aqueous thermal boundary layer. *Boundary-Layer Meteorology*, *18*(1), 107–127. <https://doi.org/10.1007/BF00117914>

Lagerloef, G., Colomb, F. R., Le Vine, D., Wentz, F., Yueh, S., Ruf, C., et al. (2008). The Aquarius/SAC-D mission: Designed to meet the salinity remote-sensing challenge. *Oceanography*, *21*(1), 68–81. <https://doi.org/10.5670/oceanog.2008.68>

Lindstrom, E., Bryan, F., & Schmitt, R. (2015). SPURS: Salinity processes in the upper-ocean regional study: The North Atlantic experiment. *Oceanography*, *28*(1), 14–19. <https://doi.org/10.5670/oceanog.2015.01>

Murray, M. J., Allen, M. R., Merchant, C. J., Harris, A. R., & Donlon, C. J. (2000). Direct observations of skin-bulk SST variability. *Geophysical Research Letters*, *27*(8), 1171–1174. <https://doi.org/10.1029/1999GL011133>

Mustafa, N. I. H., Ribas-Ribas, M., & Wurl, O. (2017). High-resolution variability of the enrichment of fluorescence dissolved organic matter in the sea surface microlayer of an upwelling region. *Elementa: Science of the Anthropocene*, *5*, 52. <https://doi.org/10.1525/elementa.242>

Phan, C. M. (2014). Stability of a floating water droplet on an oil surface. *Langmuir*, *30*(3), 768–773. <https://doi.org/10.1021/la403830k>

Phan, C. M., Allen, B., Peters, L. B., Le, T. N., & Tade, M. O. (2012). Can water float on oil? *Langmuir*, *28*(10), 4609–4613. <https://doi.org/10.1021/la204820a>

Reul, N., Fournier, S., Boutin, J., Hernandez, O., Maes, C., Chapron, B., et al. (2014). Sea surface salinity observations from space with the SMOS satellite: A new means to monitor the marine branch of the water cycle. *Surveys in Geophysics*, *35*(3), 681–722. <https://doi.org/10.1007/s10712-013-9244-0>

Reverdin, G., Morisset, S., Boutin, J., & Martin, N. (2012). Rain-induced variability of near sea-surface T and S from drifter data. *Journal of Geophysical Research*, *117*, C02032. <https://doi.org/10.1029/2011JC007549>

Ribas-Ribas, M., Hamizah Mustafa, N. I., Rahlff, J., Stolle, C., & Wurl, O. (2017). Sea surface scanner (S3): A catamaran for high-resolution measurements of biogeochemical properties of the sea surface microlayer. *Journal of Atmospheric and Oceanic Technology*, *34*(7), 1433–1448. <https://doi.org/10.1175/JTECH-D-17-0017.1>

Santos, C. F., Agardy, T., Andrade, F., Barange, M., Crowder, L. B., Ehler, C. N., et al. (2016). Ocean planning in a changing climate. *Nature Geoscience*, *9*(10), 730. <https://doi.org/10.1038/ngeo2821>

Saunders, P. M. (1967). The temperature at the ocean-air interface. *Journal of the Atmospheric Sciences*, *24*(3), 269–273. [https://doi.org/10.1175/1520-0469\(1967\)024<0269:TTATOA>2.0.CO;2](https://doi.org/10.1175/1520-0469(1967)024<0269:TTATOA>2.0.CO;2)

- Schlitzer, R. (2018). Ocean Data View, <https://odv.awi.de>
- Schlüssel, P., Emery, W. J., Grassl, H., & Mammen, T. (1990). On the bulk-skin temperature difference and its impact on satellite remote sensing of sea surface temperature. *Journal of Geophysical Research*, *95*(C8), 13,341–13,356. <https://doi.org/10.1029/JC095IC08p13341>
- Schlüssel, P., Soloviev, A. V., & Emery, W. J. (1997). Cool and freshwater skin of the ocean during rainfall. *Boundary-Layer Meteorology*, *82*(3), 439–474. <https://doi.org/10.1023/A:1000225700380>
- Shinki, M., Wendeberg, M., Vagle, S., Cullen, J. T., & Hore, D. K. (2012). Characterization of adsorbed microlayer thickness on an oceanic glass plate sampler. *Limnology and Oceanography: Methods*, *10*(10), 728–735. <https://doi.org/10.4319/lom.2012.10.728>
- Singh, P., & Joseph, D. D. (2005). Fluid dynamics of floating particles. *Journal of Fluid Mechanics*, *530*, 31–80. <https://doi.org/10.1017/S0022112005003575>
- Soloviev, A., & Lukas, R. (2013). *The near-surface layer of the ocean: structure, dynamics and applications*, (Vol. 48). Dordrecht, Netherlands: Springer Science & Business Media.
- Soloviev, A., Matt, S., & Fujimara, A. (2015). Three-dimensional dynamics of freshwater lenses in the ocean's near-surface layer. *Oceanography*, *28*(1), 142–149. <https://doi.org/10.5670/oceanog.2015.14>
- Song, Y. T., Lee, T., Moon, J. H., Qu, T., & Yueh, S. (2015). Modeling skin-layer salinity with an extended surface-salinity layer. *Journal of Geophysical Research: Oceans*, *120*, 1079–1095. <https://doi.org/10.1002/2014JC010346>
- Vinogradova, N. T., & Ponte, R. M. (2013). Small-scale variability in sea surface salinity and implications for satellite-derived measurements. *Journal of Atmospheric and Oceanic Technology*, *30*(11), 2689–2694. <https://doi.org/10.1175/JTECH-D-13-00110.1>
- Ward, B., Wanninkhof, R., Minnett, P. J., & Head, M. J. (2004). SkinDeP: A profiling instrument for upper-decameter sea surface measurements. *Journal of Atmospheric and Oceanic Technology*, *21*(2), 207–222. [https://doi.org/10.1175/1520-0426\(2004\)021<0207:SAPIFU>2.0.CO;2](https://doi.org/10.1175/1520-0426(2004)021<0207:SAPIFU>2.0.CO;2)
- Webster, P. J. (1994). The role of hydrological processes in ocean-atmosphere interactions. *Reviews of Geophysics*, *32*(4), 427–476. <https://doi.org/10.1029/94RG01873>
- Wurl, O., Bird, K., Cunliffe, M., Landing, W. M., Miller, U., Mustafa, N. I. H., et al. (2018). Warming and inhibition of salinization at the ocean's surface by cyanobacteria. *Geophysical Research Letters*, *45*, 4230–4237. <https://doi.org/10.1029/2018GL077946>
- Wurl, O., Ekau, W., Landing, W. M., & Zappa, C. J. (2017). Sea surface microlayer in a changing ocean—A perspective. *Elementa: Science of the Anthropocene*, *5*, 31. <https://doi.org/10.1525/elementa.228>
- Wurl, O., Mustafa, N. I. H., & Ribas-Ribas, M. (2017). *Multiparameter measurement of biochemical properties of the sea surface microlayer in the Pacific Ocean during R/V Falkor cruise FK161010*, Edited. Bremen, Germany: PANGAEA. <https://doi.pangaea.de/10.1594/PANGAEA.882430>
- Wurl, O., Wurl, E., Miller, L., Johnson, K., & Vagle, S. (2011). Formation and global distribution of sea-surface microlayers. *Biogeosciences*, *8*(1), 121–135. <https://doi.org/10.5194/bg-8-121-2011>
- Yu, L. (2010). On sea surface salinity skin effect induced by evaporation and implications for remote sensing of ocean salinity. *Journal of Physical Oceanography*, *40*(1), 85–102. <https://doi.org/10.1175/2009JPO4168.1>
- Zappa, C. J., Asher, W. E., & Jessup, A. T. (2001). Microscale wave breaking and air-water gas transfer. *Journal of Geophysical Research*, *106*(C5), 9385–9391. <https://doi.org/10.1029/2000JC000262>
- Zappa, C. J., Asher, W. E., Jessup, A. T., Klinke, J., & Long, S. R. (2004). Microbreaking and the enhancement of air-water transfer velocity. *Journal of Geophysical Research*, *109*, C08S16. <https://doi.org/10.1029/2003JC001897>
- Zappa, C. J., Banner, M. L., Schultz, H., Corrada-Emmanuel, A., Wolff, L. B., & Yalcin, J. (2008). Retrieval of short ocean wave slope using polarimetric imaging. *Measurement Science and Technology*, *19*(5), 055503. <https://doi.org/10.1088/0957-0233/19/5/055503>
- Zappa, C. J., Banner, M. L., Schultz, H., Gemmrich, J. R., Morison, R. P., LeBel, D. A., & Dickey, T. (2012). An overview of sea state conditions and air-sea fluxes during RaDyO. *Journal of Geophysical Research*, *117*, C00H19. <https://doi.org/10.1029/2011JC007336>
- Zappa, C. J., Ho, D. T., McGillis, W. R., Banner, M. L., Dacey, J. W., Bliven, L. F., Ma, B., et al. (2009). Rain-induced turbulence and air-sea gas transfer. *Journal of Geophysical Research*, *114*, C07009. <https://doi.org/10.1029/2008JC005008>
- Zappa, C. J., Jessup, A. T., & Yeh, H. (1998). Skin layer recovery of free-surface wakes: Relationship to surface renewal and dependence on heat flux and background turbulence. *Journal of Geophysical Research*, *103*(C10), 21,711–21,722. <https://doi.org/10.1029/98JC01942>
- Zhang, Y., & Zhang, X. (2012). Ocean haline skin layer and turbulent surface convections. *Journal of Geophysical Research*, *117*, C04017. <https://doi.org/10.1029/2011JC007464>